

ORSIFlow: Saliency-Guided Rectified Flow for Optical Remote Sensing Salient Object Detection

Haojing Chen^{1,2}, Zhihang Liu², Yutong Li^{2,3}, Tao Tan², Haoyu Bian², Qiuju Ma¹✉

¹China University of Mining & Technology (Beijing), Beijing, China

²University of Electronic Science and Technology of China, Chengdu, China

³Hainan University, Haikou, China

Abstract—Optical Remote Sensing Image Salient Object Detection (ORSI-SOD) remains challenging due to complex backgrounds, low contrast, irregular object shapes, and large variations in object scale. Existing discriminative methods directly regress saliency maps, while recent diffusion-based generative approaches suffer from stochastic sampling and high computational cost. In this paper, we propose ORSIFlow, a saliency-guided rectified flow framework that reformulates ORSI-SOD as a deterministic latent flow generation problem. ORSIFlow performs saliency mask generation in a compact latent space constructed by a frozen variational autoencoder, enabling efficient inference with only a few steps. To enhance saliency awareness, we design a Salient Feature Discriminator for global semantic discrimination and a Salient Feature Calibrator for precise boundary refinement. Extensive experiments on multiple public benchmarks show that ORSIFlow achieves state-of-the-art performance with significantly improved efficiency. Codes are available at: <https://github.com/Ch3nSir/ORSIFlow>.

Index Terms—Salient Object Detection, Optical Remote Sensing Image, Flow Matching

I. INTRODUCTION

Salient Object Detection (SOD) aims to identify the most visually salient objects in a scene and has been widely applied in many fields [1]–[4]. With the increasing availability of Optical Remote Sensing Images (ORSIs) in fields including geography, agriculture, and security surveillance, Optical Remote Sensing Image Salient Object Detection (ORSI-SOD) has attracted growing research attention.

ORSIs are typically captured from high-altitude sensors and often contain complex and cluttered backgrounds, where salient objects exhibit strong visual similarity to their surroundings in terms of texture, color, or structural patterns [5]–[7]. These challenges are further aggravated by irregular object topologies (e.g., meandering rivers and irregular coastlines), low object-to-background contrast, extreme scale variations, and dense small structures such as vehicles. Most existing ORSI-SOD methods adopt a discriminative learning paradigm that directly predicts saliency maps from input images. For instance, Li *et al.* [8] proposed LVNet, which employs a nested architecture and dual-stream pyramids to integrate multi-level features. Li *et al.* [9] exploits global contextual information for ORSI-SOD into the transformer models. To enhance the

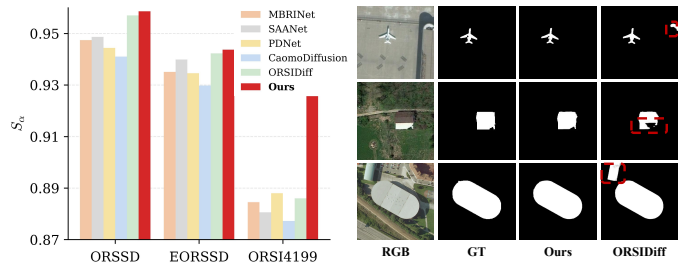


Fig. 1. The left panel shows performance in terms of S_α on three datasets, while the right panel compares our method against a previous state-of-the-art approach. Red boxes indicate segmentation errors.

capability of transformer, Zhou *et al.* [10] incorporates edge-aware attention mechanism and Li *et al.* [11] coordinate contextual information across adjacent feature levels. Furthermore, Gu *et al.* [12] introduces feature learning to efficiently aggregate fine-grained and semantic features, while Di *et al.* [13] employ adaptive weighting strategies for multiscale feature aggregation.

Recent studies have explored generative formulations that treat saliency detection as a mask generation problem. For example, Han *et al.* [14] introduces diffusion models into ORSI-SOD and achieves encouraging results by iteratively refining noisy masks. However, diffusion models typically rely on stochastic and curved denoising trajectories in the pixel space, requiring a large number of sampling steps, which limit the reasoning efficiency. As illustrated in Fig. 1, such stochastic generation may still struggle to preserve fine-grained structures and small salient objects, leading to fragmented boundaries or background interference. Moreover, saliency masks exhibit relatively structured and low-entropy distributions, suggesting that a more controllable and deterministic generation process may suffice. This observation motivates us to reconsider ORSI-SOD from a flow-based perspective.

In this paper, we propose ORSIFlow, which reformulates ORSI-SOD as a saliency-guided latent flow matching problem. Instead of performing generation in the pixel space, ORSIFlow conducts mask generation in a compact latent space constructed by a variational autoencoder, significantly reducing computational complexity. Built upon this latent representation, a rectified flow model learns a deterministic and approximately linear transformation between noise and saliency masks, enabling high-quality prediction with only

✉ Corresponding author: ma200609@126.com

This work was supported by the Fundamental Research Funds for the Central Universities.

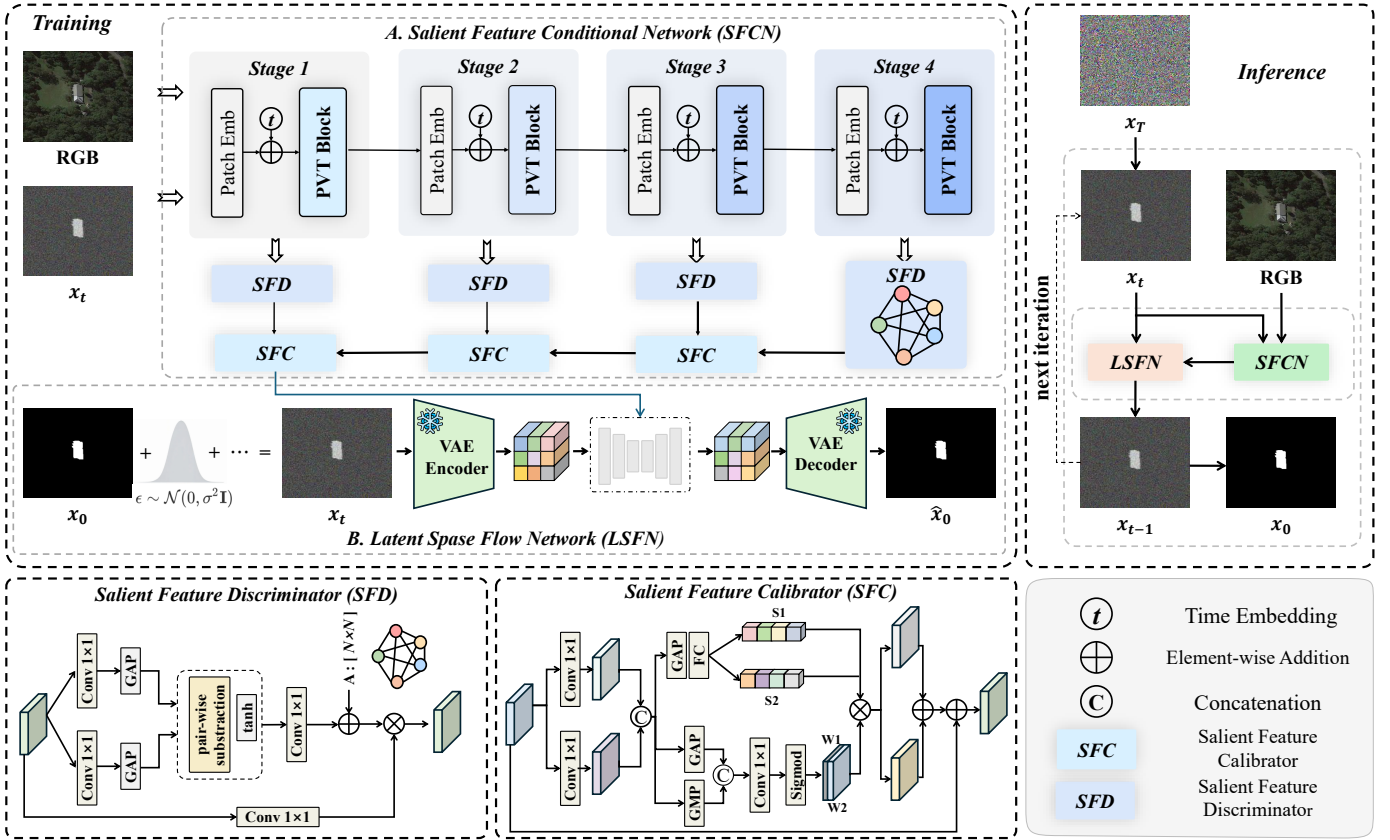


Fig. 2. Overall architecture of the proposed method. The SFCN extracts multi-scale conditional features via SFD and SFC modules, while the LSFN learns a deterministic velocity field to transform the Gaussian distribution into saliency maps within the VAE latent space.

a few inference steps. Furthermore, we introduce explicit saliency guidance through the Salient Feature Discriminator (SFD) and the Salient Feature Calibrator (SFC). Inspired by [15], the SFD constructs a dynamic graph topology to characterize global semantic dependencies through channel-wise reasoning. The SFC is inspired by [4], which possesses the characteristic of Spatial-Spectral Selection, and is specifically designed for small objects and complex boundaries in object detection tasks. Concurrently, the SFC utilizes a dual-branch gating mechanism to dynamically aggregate local and contextual information via adaptive feature modulation. Extensive experiments on multiple public ORSI-SOD benchmarks demonstrate that ORSIFlow achieves superior performance while substantially reducing computational cost, validating the effectiveness of the proposed approach.

Our contributions are summarized as follows:

- We propose ORSIFlow, a saliency-guided rectified flow framework, which performs saliency mask generation instead of direct discriminative prediction.
- We generate saliency masks in a compact latent space built by a frozen variational autoencoder and use rectified flow to map noise to masks, enabling stable training and efficient inference with few steps.
- We design two specialized guidance modules to enhance the generative quality: the Salient Feature Discriminator (SFD) effectively eliminates semantic ambiguity to

maintain global consistency, while the Salient Feature Calibrator (SFC) guarantees precise boundary delineation for objects with extreme scale variations.

- Extensive experiments on multiple public ORSI-SOD benchmarks demonstrate the effectiveness of ORSIFlow.

II. RELATED WORK

ORSI-SOD. Early ORSI-SOD methods primarily relied on CNNs, achieving progress through multi-scale feature aggregation and nested architectures [8]. With the rise of self-attention, Transformers and Mamba-based modules were introduced to capture long-range dependencies and global context [9] [5] [16]. Recently, generative formulations like diffusion models have emerged to iteratively refine masks from noise [17] [14]. However, these methods either lack explicit progressive refinement or suffer from the high computational cost and instability of pixel-space diffusion, often struggling to balance boundary preservation with efficient inference in complex remote sensing scenes.

Flow-Based Generative Learning. Leverages continuous normalizing flows (CNFs) to model a probability flow from a simple prior to the target data distribution. Lipman et al. [18] introduced flow matching for CNFs, learning a vector field along a fixed conditional probability path, enabling simulation-free training and generalizing diffusion paths. Compared with diffusion models, which rely on stochastic pixel-space denoising and incur high sampling costs, Rectified

Flow [19] learns velocity fields along straight trajectories, simplifying inference and enabling few-step sampling.

III. METHODOLOGY

A. Overall Architecture

As illustrated in Fig. 2, our overall architecture consists of a Salient Feature Conditional Network and a Latent Space Flow Network. The Salient Feature Conditional Network first employs a four-stage PVTv2-b4 hierarchy to progressively extract multi-scale fused features by integrating RGB cues with the mask representation. Based on these fused features, the Salient Feature Discriminator performs relational modeling of global semantics, while the Salient Feature Calibrator corrects local details to enhance fine structures and boundary quality, yielding salient features. Then, the Latent Space Flow Network takes the salient features as conditional input and performs iterative updates in a low-dimensional latent space compressed by a VAE, finally producing the predicted saliency map.

B. Salient Feature Conditional Network

We design the Salient Feature Conditional Network (SFCN), as shown in Fig. 2(A), based on a four-stage pyramid Transformer backbone to extract hierarchical conditional features. Each stage follows a PVT-style architecture, where the spatial resolution is progressively reduced while the level of semantic abstraction is gradually increased. Given the input RGB image I and the noisy saliency mask X_t , the stage-wise embeddings are constructed as

$$OP_n = \begin{cases} \text{Conv}(\mathcal{R}(\text{Conv}(I) + \text{Conv}(X_t))) & n = 1, \\ \text{Conv}(\mathcal{R}(\text{Conv}(OP_{n-1}))) & n = 2, 3, 4. \end{cases} \quad (1)$$

where OP_n denotes the stage-wise embedding at stage n , constructed from the RGB image I and the noisy saliency mask X_t via convolutional projection and patch reshaping.

To adapt conditional features to different flow time steps, the continuous time variable $t \in [0, 1]$ is encoded with a sinusoidal positional embedding.

$$T = \text{SPE}(t), \quad t \sim \mathcal{U}(0, 1), \quad (2)$$

where $\text{SPE}(\cdot)$ is the sinusoidal positional embedding. The time embedding is injected into Transformer blocks at each stage, yielding temporally-aware multi-scale features $\{F_n\}_{n=1}^4$, where F_n denotes the output feature of the n -th Transformer stage.

Given the multi-scale conditional features $\{F_n\}_{n=1}^4$, we apply a Salient Feature Discriminator (SFD) followed by a Salient Feature Calibrator (SFC) in a stage-wise manner to progressively refine features at different semantic levels. For the challenges in the ORSI-SOD task, where tiny objects are difficult to detect and complex boundaries are hard to determine, we propose the SFC module. Specifically, we replace the large-kernel convolution in [4] with a 1×1 convolution, and redesign the average pooling and max pooling operations

into a dual-branch structure, enabling the model to capture finer-grained objects more effectively.

SFD aims to enhance target-background separability. We generate an importance map based on the difference between two projected channel descriptors:

$$z_1, z_2 = \text{GAP}(\text{Conv}_{1 \times 1}(\mathbf{F})), \quad (3)$$

$$\mathbf{A} = \sigma(\text{Conv}_{1 \times 1}(\tanh(z_1 - z_2))), \quad (4)$$

where \ominus denotes the pair-wise subtraction operation. Concurrently, the original feature \mathbf{F} is mapped to a node feature representation via a third 1×1 convolution. We then perform graph convolution over \mathcal{G} to propagate relational context across channel nodes [15]. By incorporating an identity matrix \mathbf{I} to retain self-loops, the graph reasoning process is formulated as:

$$\mathbf{F}_{\text{SFD}} = (\mathbf{A} + \mathbf{I}) \otimes \text{Conv}_{1 \times 1}(\mathbf{F}) \quad (5)$$

where \otimes denotes matrix multiplication.

Building upon \mathbf{F}_{SFD} , SFC adopts a dual-branch projection with dual-gating fusion to improve structural fidelity in remote-sensing imagery. Specifically, \mathbf{F}_{SFD} is projected into two feature branches via separate 1×1 convolutions, $\mathbf{F}_1 = \text{Conv}_{1 \times 1}(\mathbf{F}_{\text{SFD}})$, with \mathbf{F}_2 obtained similarly. The two branches are then concatenated to form the fused feature:

$$\mathbf{F}_c = \text{Concat}(\mathbf{F}_1, \mathbf{F}_2). \quad (6)$$

We then exploit complementary global statistics from \mathbf{F}_c : average pooling captures the overall response distribution, while max pooling highlights sparse yet strong activations typical for small objects and thin boundaries,

$$\mathbf{g}_{\text{avg}} = \text{GAP}(\mathbf{F}_c), \quad \mathbf{g}_{\text{max}} = \text{GMP}(\mathbf{F}_c). \quad (7)$$

These statistics are fused to produce dual calibration gates for the two branches,

$$\mathbf{W}_1, \mathbf{W}_2 = \text{Split}(\sigma(\text{Conv}_{1 \times 1}(\text{Concat}(\mathbf{g}_{\text{avg}}, \mathbf{g}_{\text{max}})))). \quad (8)$$

A channel-attention branch generates dual channel-wise scaling factors:

$$\mathbf{s}_1, \mathbf{s}_2 = \text{Split}(\text{FC}(\text{GAP}(\mathbf{F}_c))). \quad (9)$$

Finally, SFC performs dual-gating fusion with a residual formulation:

$$\mathbf{F}_{\text{cond}} = \mathbf{W}_1 \otimes \mathbf{s}_1 + \mathbf{W}_2 \otimes \mathbf{s}_2 + \mathbf{F}_{\text{SFD}}. \quad (10)$$

In remote sensing scenes, salient objects often appear at varying scales with weak boundaries. By jointly exploiting average and extreme responses with dual-branch gating, SFC enhances small-scale yet informative regions, thereby improving saliency localization accuracy.

TABLE I

QUANTITATIVE COMPARISON RESULTS IN TERMS OF F_{β}^{max} , E_{ξ}^{max} , S_{α} AND MAE SCORE ARE PRESENTED ON THREE BENCHMARK DATASETS. IN THE TABLES, \uparrow AND \downarrow INDICATE THAT HIGHER AND LOWER VALUES ARE PREFERRED, RESPECTIVELY. THE TOP THREE RESULTS IN EACH COLUMN ARE HIGHLIGHTED IN RED, BLUE, AND GREEN, RESPECTIVELY.

Method	Pub	ORSSD				EORSSD				ORSI-4199			
		$S_{\alpha} \uparrow$	$F_{\beta}^{max} \uparrow$	$E_{\xi}^{max} \uparrow$	$MAE \downarrow$	$S_{\alpha} \uparrow$	$F_{\beta}^{max} \uparrow$	$E_{\xi}^{max} \uparrow$	$MAE \downarrow$	$S_{\alpha} \uparrow$	$F_{\beta}^{max} \uparrow$	$E_{\xi}^{max} \uparrow$	$MAE \downarrow$
GeleNet [20]	TIP-23	0.9328	0.9109	0.9760	0.0099	0.9324	0.8796	0.9735	0.0063	0.8730	0.8663	0.9397	0.0318
ACCoNet [21]	TCYB-23	0.9437	0.9149	0.9796	0.0080	0.9290	0.8837	0.9727	0.0074	0.8817	0.8740	0.9478	0.0294
ERPNet [10]	TCYB-23	0.9352	0.9036	0.9738	0.0114	0.9252	0.8743	0.9665	0.0082	0.8684	0.8610	0.9384	0.0327
WeightNet [22]	TGRS-24	0.9512	0.9278	0.9864	0.0075	0.9417	0.8908	0.9809	0.0060	0.8868	0.8821	0.9496	0.0290
PRNet [12]	TGRS-24	0.9425	0.9153	0.9866	0.0068	0.9296	0.8707	0.9809	0.0053	0.8795	0.8734	0.9491	0.0280
RAGRNet [17]	TGRS-24	0.9507	0.9242	0.9861	0.0066	0.9361	0.8852	0.9788	0.0057	0.8859	0.8803	0.9490	0.0281
CamoDiff [23]	TPAMI-25	0.9410	0.9116	0.9779	0.0096	0.9298	0.8809	0.9685	0.0075	0.8772	0.8710	0.9432	0.0312
MRBNet [6]	TGRS-25	0.9474	0.9199	0.9851	0.0069	0.9351	0.8852	0.9766	0.0056	0.8845	0.8787	0.9489	0.0287
SAANet [5]	EAAI-25	0.9487	0.9226	0.9840	0.0078	0.9399	0.8918	0.9801	0.0057	0.8806	0.8773	0.9455	0.0302
PDNet [16]	EAAI-25	0.9444	0.9161	0.9668	0.0080	0.9346	0.8813	0.9524	0.0063	0.8880	0.8755	0.9554	0.0270
ORSIDiff [14]	TGRS-25	0.9570	0.9255	0.9880	0.0054	0.9423	0.8890	0.9830	0.0046	0.8860	0.8812	0.9510	0.0275
Ours	—	0.9586	0.9262	0.9883	0.0050	0.9437	0.9010	0.9840	0.0041	0.8935	0.8870	0.9545	0.0262

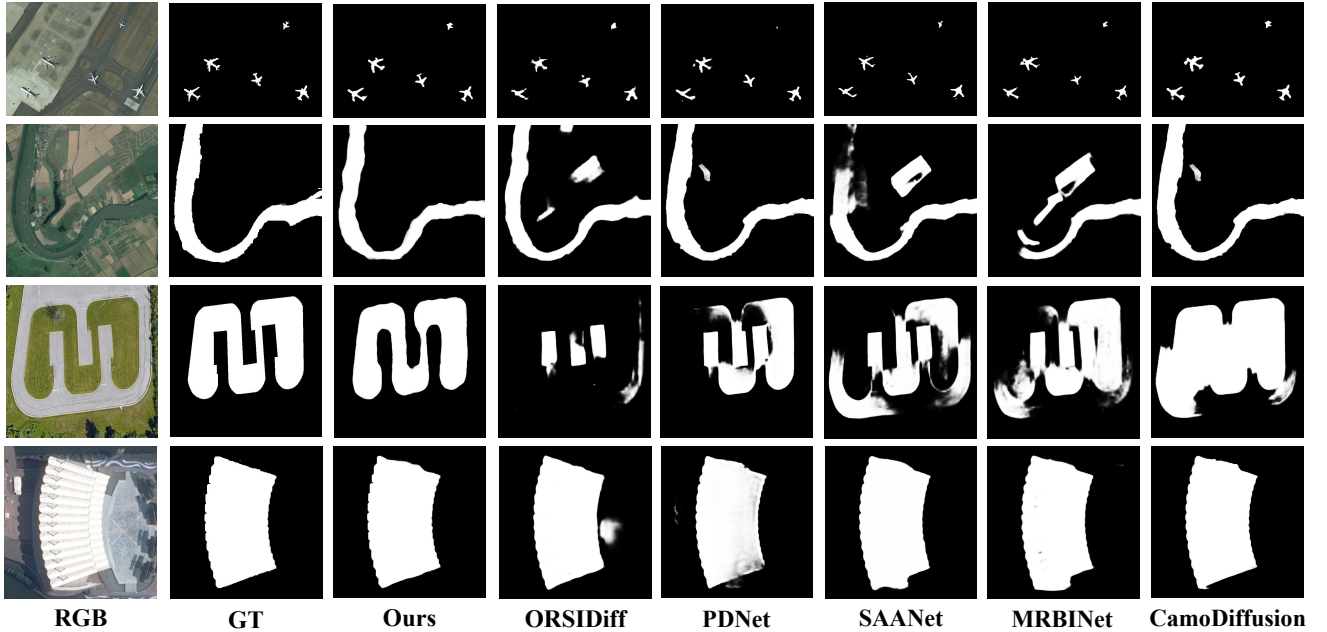


Fig. 3. Qualitative comparison of ORSIFlow and other state-of-the-art methods

C. Latent Space Flow Network

The Latent Space Flow Network (LSFN), as shown in Fig. 2(B), performs saliency-conditioned modeling in a compact latent space provided by a Variational Autoencoder (VAE). During training, we first construct the noisy saliency map in the image space. Specifically, given the clean saliency map \mathbf{x}_0 and a Gaussian noise sample $\epsilon_x \sim \mathcal{N}(\mathbf{0}, \mathbf{I})$, the noisy state at time step $t \in [0, 1]$ is defined as:

$$\mathbf{x}_t = (1 - t)\mathbf{x}_0 + t\epsilon_x. \quad (11)$$

The noisy saliency map \mathbf{x}_t is then mapped into the latent space through the VAE encoder:

$$\mathbf{z}_t = E(\mathbf{x}_t), \quad (12)$$

where $E(\cdot)$ denotes the VAE encoder, and \mathbf{z}_t represents the latent representation of the noisy state.

Conditioned on the saliency-aware embedding \mathbf{F}_{cond} , LSFN adopts Rectified Flow to learn a deterministic velocity field \mathbf{v}_{θ} in the latent space:

$$\frac{d\mathbf{z}_t}{dt} = \mathbf{v}_{\theta}(\mathbf{z}_t, t, \mathbf{F}_{\text{cond}}). \quad (13)$$

Therefore, the latent state \mathbf{z}_t is induced by encoding the noisy saliency map \mathbf{x}_t , rather than by directly interpolating between a clean latent code and Gaussian noise in the latent space. The network parameters are optimized by minimizing the mean squared error between the predicted velocity and the target direction ($\epsilon - \mathbf{z}_0$):

$$\mathcal{L}_{\text{RF}} = \mathbb{E}_{\mathbf{z}_0, \epsilon, t} \|\mathbf{v}_{\theta}(\mathbf{z}_t, t, \mathbf{F}_{\text{cond}}) - (\epsilon - \mathbf{z}_0)\|_2^2. \quad (14)$$

Finally, the refined latent representation $\hat{\mathbf{z}}_0$ (obtained after solving the flow ODE) is reconstructed to produce the prediction:

$$\hat{\mathbf{x}} = D(\hat{\mathbf{z}}_0), \quad (15)$$

TABLE II

COMPARISON OF DIFFERENT MODULE ABLATION SETTINGS ON ORSSD, EORSSD AND ORSI-4199 DATASETS. THE BEST RESULT IN EACH COLUMN IS HIGHLIGHTED IN BOLD.

NO.	Module Ablation			ORSSD (200 test images)				EORSSD (600 test images)				ORSI-4199 (2199 test images)			
	VAE	SFD	SFC	$S_\alpha \uparrow$	$F_\beta^{max} \uparrow$	$E_\xi^{max} \uparrow$	$MAE \downarrow$	$S_\alpha \uparrow$	$F_\beta^{max} \uparrow$	$E_\xi^{max} \uparrow$	$MAE \downarrow$	$S_\alpha \uparrow$	$F_\beta^{max} \uparrow$	$E_\xi^{max} \uparrow$	$MAE \downarrow$
(a)				0.9453	0.9003	0.9841	0.0063	0.9303	0.8846	0.9787	0.0051	0.8696	0.8593	0.9437	0.0302
(b)	✓			0.9479	0.9067	0.9847	0.0061	0.9326	0.8882	0.9794	0.0050	0.8740	0.8651	0.9461	0.0297
(c)		✓		0.9548	0.9189	0.9863	0.0056	0.9398	0.8970	0.9821	0.0046	0.8866	0.8789	0.9515	0.0274
(d)			✓	0.9516	0.9128	0.9856	0.0059	0.9362	0.8923	0.9811	0.0048	0.8801	0.8724	0.9492	0.0287
(e)	✓	✓		0.9567	0.9217	0.9875	0.0052	0.9415	0.8989	0.9831	0.0044	0.8894	0.8826	0.9530	0.0271
(f)	✓		✓	0.9534	0.9150	0.9860	0.0057	0.9377	0.8941	0.9817	0.0047	0.8832	0.8752	0.9504	0.0281
(g)		✓	✓	0.9578	0.9246	0.9874	0.0052	0.9426	0.9002	0.9831	0.0043	0.8917	0.8846	0.9534	0.0268
(h)	✓	✓	✓	0.9586	0.9262	0.9883	0.0050	0.9437	0.9010	0.9840	0.0041	0.8935	0.8870	0.9545	0.0262

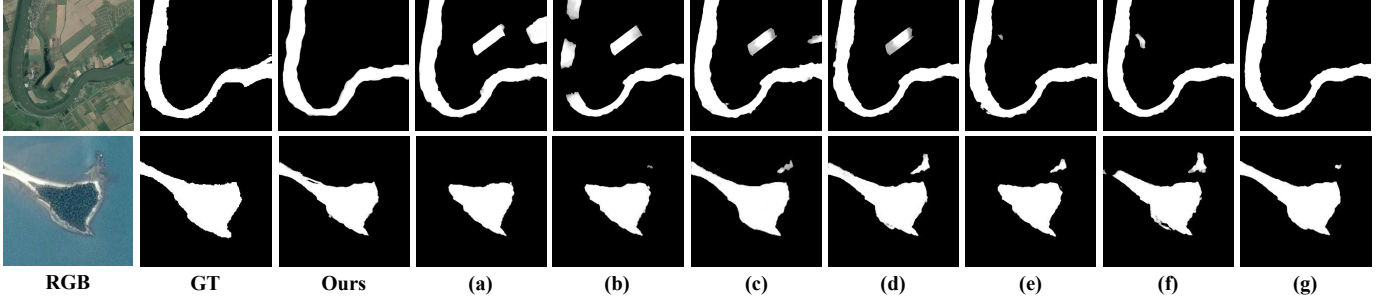


Fig. 4. Visual results of the effectiveness of our modules.

where $D(\cdot)$ denotes the decoder, and \hat{x} is the final predicted saliency map. At inference time, we update the latent variable for a few steps before decoding, as illustrated in Fig. 2.

IV. EXPERIMENT

A. Experimental Setup

Implementation Details. The proposed model is implemented using the publicly available PyTorch framework and a single NVIDIA GeForce H100 GPU. During both the training and testing, all input images are resized to 352×352. We trained our model for 150 epochs using the AdamW optimizer with a batch size of 32 and an initial learning rate of 1e-4.

Datasets. We conduct experiments on three widely-used datasets for ORSI-SOD: ORSSD [8], EORSSD [7] and ORSI-4199 [24]. The ORSSD dataset comprises 800 image pairs, with 600 pairs allocated for training and the remaining 200 for testing. The EORSSD dataset, an extended version of ORSSD, contains 2000 image pairs, of which 1400 are used for training and 600 for testing. The ORSI-4199 dataset consists of 2000 training samples and 2199 testing samples, and is widely regarded as the most challenging benchmark in ORSI-SOD due to its diverse and complex scenes.

Evaluation Metrics. We employed four widely used metrics to quantitatively evaluate the performance of all the methods, including S-measure (S_α) [25], Mean Absolute Error (MAE), maximum E-measure (E_ξ^{max}) [26], and maximum F-measure (F_β^{max}).

B. Performance Comparison

We conduct comparison between our proposed method and eleven other state-of-the-art (SOTA) methods, including GeleNet [20], ACCoNet [21], ERPNet [10], WeightNet [22],

PRNet [12], RAGRNet [17], CamoDiff [23], MRBNet [6], SAANet [5], PDNet [16] and ORSIDiff [14]. To ensure a fair evaluation, the prediction results for all competing models were generated using their officially released open-source code and recommended parameter settings.

Quantitative Comparison. As shown in Table I, our method consistently outperforms existing SOTA approaches on three datasets under four evaluation metrics. On ORSSD, our method achieves the highest F_β^{max} , S_α and E_ξ^{max} , together with the lowest MAE, reflecting accurate and structurally consistent predictions. Similar trends can be observed on EORSSD, where our approach ranks first on all metrics, demonstrating its strong generalization capability. Although ORSI-4199 is more challenging due to complex backgrounds and diverse object scales, our method remains highly competitive against existing methods.

Qualitative Comparison. Fig.3 presents qualitative comparisons between our method and several representative state-of-the-art methods. In the first row, most competing methods fail to detect small objects or miss part of the objects, whereas our method achieves more complete detections. In the second and third rows, which contain thin and elongated structures, several methods produce fragmented predictions or inaccurate boundaries, while our method better preserves the overall object structure. In the last row, where background clutter and low contrast pose additional challenges, existing approaches generate noticeable false positives, whereas our method produces cleaner segmentation results.

C. Ablation Studies

We conduct ablation studies on ORSSD, EORSSD, and ORSI-4199 to evaluate the effectiveness of each module.

As reported in Table II, introducing individual components consistently improves performance in terms of F_{β}^{max} , S_{α} , E_{ξ}^{max} and MAE, while combining them leads to further gains. The full model achieves the best overall results across all datasets. Fig. 3 provides qualitative comparisons, where removing certain modules results in incomplete or fragmented predictions, whereas the full model produces more accurate and coherent segmentation results.

D. Efficiency Analysis

TABLE III

EFFICIENCY COMPARISON ON THE ORSI-4199 DATASET WITH DIFFERENT TIME STEPS AMONG GENERATIVE ORSI-SOD METHODS. THE BEST RESULT IN EACH COLUMN IS HIGHLIGHTED IN BOLD.

Method	Timestep	FLOPs (G)	FPS	$S_{\alpha} \uparrow$	$F_{\beta}^{max} \uparrow$	$E_{\xi}^{max} \uparrow$	$MAE \downarrow$
CamoDiff	10	60.29	0.3	0.8772	0.8710	0.9432	0.0312
ORSIDiff	10	15.25	8	0.8860	0.8812	0.9510	0.0275
Ours	3	5.68	19	0.8935	0.8870	0.9545	0.0262

Table III compares the efficiency and performance of different generative ORSI-SOD methods on the ORSI-4199 dataset. Our method achieves a superior efficiency–accuracy trade-off by using significantly fewer diffusion steps and FLOPs, while delivering the highest inference speed on GPU. Meanwhile, it attains the best overall performance in terms of S_{α} , F_{β}^{max} , and E_{ξ}^{max} , along with the lowest MAE , demonstrating its effectiveness and computational efficiency.

V. CONCLUSION

ORSIFlow is a saliency-guided rectified flow framework for optical remote sensing salient object detection. By generating saliency masks in a compact latent space and using deterministic rectified flow, it achieves accurate predictions efficiently. The Salient Feature Discriminator and Calibrator enhance global semantic discrimination and boundary precision. Experiments on public benchmarks show ORSIFlow outperforms state-of-the-art methods with fewer inference steps, demonstrating the promise of flow-based generative modeling for robust and efficient remote sensing saliency detection.

REFERENCES

- [1] Bo Yu and Fang Chen, “Large-scale landslide detection for practical use based on image saliency,” *Journal of Applied Remote Sensing*, vol. 10, no. 4, pp. 045013, 2016.
- [2] Mengyu Ren, Yutong Li, Hua Li, Chuhong Wang, and Runmin Cong, “Beyond global scanning: Adaptive visual state space modeling for salient object detection in optical remote sensing images,” 2026.
- [3] Runtong Li, Shijie Lian, Hua Li, Yutong Li, Wenhui Wu, and Sam Kwong, “Waterflow: Explicit physics-prior rectified flow for underwater saliency mask generation,” 2026.
- [4] Yichu Xu, Di Wang, Lefei Zhang, and Liangpei Zhang, “Dual selective fusion transformer network for hyperspectral image classification,” 2025.
- [5] Yanliang Ge, Taichuan Liang, Junchao Ren, Min He, Hongbo Bi, and Qiao Zhang, “Semantic awareness aggregation for salient object detection in remote sensing images,” *Engineering Applications of Artificial Intelligence*, vol. 160, pp. 111837, 2025.
- [6] Yun Jia, Jie Zhao, Lin Ma, and Lidan Yu, “Multistrategy region and boundary interaction network for salient object detection in optical remote sensing images,” *IEEE Transactions on Geoscience and Remote Sensing*, vol. 63, pp. 1–16, 2025.
- [7] Qijian Zhang, Runmin Cong, Chongyi Li, Ming-Ming Cheng, Yuming Fang, Xiaochun Cao, Yao Zhao, and Sam Kwong, “Dense attention fluid network for salient object detection in optical remote sensing images,” *IEEE Transactions on Image Processing*, vol. 30, pp. 1305–1317, 2021.
- [8] Chongyi Li, Runmin Cong, Junhui Hou, Sanyi Zhang, Yue Qian, and Sam Kwong, “Nested network with two-stream pyramid for salient object detection in optical remote sensing images,” *IEEE Transactions on Geoscience and Remote Sensing*, vol. 57, no. 11, pp. 9156–9166, 2019.
- [9] Gongyang Li, Zhen Bai, Zhi Liu, Xinpeng Zhang, and Haibin Ling, “Salient object detection in optical remote sensing images driven by transformer,” *IEEE Transactions on Image Processing*, vol. 32, pp. 5257–5269, 2023.
- [10] Xiaofei Zhou, Kunye Shen, Li Weng, Runmin Cong, Bolun Zheng, Jiyong Zhang, and Chenggang Clarence Yan, “Edge-guided recurrent positioning network for salient object detection in optical remote sensing images,” *IEEE Transactions on Cybernetics*, vol. 53, pp. 539–552, 2022.
- [11] G. Li, Z. Liu, D. Zeng, W. Lin, and H. Ling, “Adjacent context coordination network for salient object detection in optical remote sensing images,” *IEEE Transactions on Cybernetics*, vol. 53, no. 1, pp. 526–538, 2022.
- [12] Shengyu Gu, Yong Song, Ya Zhou, Yashuo Bai, Xin Yang, and Yuxin He, “Prnet: Parallel refinement network with group feature learning for salient object detection in optical remote sensing images,” *IEEE Geoscience and Remote Sensing Letters*, vol. 21, pp. 1–5, 2024.
- [13] L. Di, B. Zhang, and Y. Wang, “Multi-scale and multi-dimensional weighted network for salient object detection in optical remote sensing images,” *IEEE Transactions on Geoscience and Remote Sensing*, vol. 62, pp. 1–16, 2024.
- [14] Jinyu Han, Jing Sun, Fasheng Wang, Fuming Sun, and Haojie Li, “Orsidiff: Diffusion model for salient object detection in optical remote sensing images,” *IEEE Transactions on Geoscience and Remote Sensing*, vol. 63, pp. 1–15, 2025.
- [15] Yuxin Chen, Ziqi Zhang, Chunfeng Yuan, Bing Li, Ying Deng, and Weiming Hu, “Channel-wise topology refinement graph convolution for skeleton-based action recognition,” 2021.
- [16] Chaojun Cen, Fei Li, Zhenbo Li, and Yun Wang, “Towards salient object detection via parallel dual-decoder network,” *Engineering Applications of Artificial Intelligence*, vol. 139, pp. 109638, 2025.
- [17] Jie Zhao, Yun Jia, Lin Ma, and Lidan Yu, “Recurrent adaptive graph reasoning network with region and boundary interaction for salient object detection in optical remote sensing images,” *IEEE Transactions on Geoscience and Remote Sensing*, vol. 62, pp. 1–20, 2024.
- [18] Yaron Lipman, Ricky TQ Chen, Heli Ben-Hamu, Maximilian Nickel, and Matt Le, “Flow matching for generative modeling,” *arXiv preprint arXiv:2210.02747*, 2022.
- [19] Xingchao Liu, Chengyue Gong, and Qiang Liu, “Flow straight and fast: Learning to generate and transfer data with rectified flow,” *arXiv preprint arXiv:2209.03003*, 2022.
- [20] Gongyang Li, Zhen Bai, Zhi Liu, Xinpeng Zhang, and Haibin Ling, “Salient object detection in optical remote sensing images driven by transformer,” *IEEE Transactions on Image Processing*, vol. 32, pp. 5257–5269, 2023.
- [21] Gongyang Li, Zhi Liu, Dan Zeng, Weisi Lin, and Haibin Ling, “Adjacent context coordination network for salient object detection in optical remote sensing images,” *IEEE Transactions on Cybernetics*, vol. 53, no. 1, pp. 526–538, 2023.
- [22] Lamei Di, Bin Zhang, and Yiming Wang, “Multiscale and multidimensional weighted network for salient object detection in optical remote sensing images,” *IEEE Transactions on Geoscience and Remote Sensing*, vol. 62, pp. 1–14, 2024.
- [23] Ke Sun, Zhongxi Chen, Xianming Lin, Xiaoshuai Sun, Hong Liu, and Rongrong Ji, “Conditional diffusion models for camouflaged and salient object detection,” *IEEE Transactions on Pattern Analysis and Machine Intelligence*, vol. 47, no. 4, pp. 2833–2848, 2025.
- [24] Zhengzheng Tu, Chao Wang, Chenglong Li, Minghao Fan, Haifeng Zhao, and Bin Luo, “Orsi salient object detection via multiscale joint region and boundary model,” *IEEE Transactions on Geoscience and Remote Sensing*, vol. 60, pp. 1–13, 2022.
- [25] Deng-Ping Fan, Ming-Ming Cheng, Yun Liu, Tao Li, and Ali Borji, “Structure-Measure: A New Way to Evaluate Foreground Maps,” in *Proceedings of the IEEE International Conference on Computer Vision (ICCV)*, 2017, pp. 4548–4557.
- [26] Deng-Ping Fan, Cheng Gong, Yang Cao, Bo Ren, Ming-Ming Cheng, and Ali Borji, “Enhanced-alignment Measure for Binary Foreground Map Evaluation,” in *Proceedings of the Twenty-Seventh International Joint Conference on Artificial Intelligence (IJCAI)*, 2018, pp. 698–704.